

Modal Transformation Method for Deformable Membrane Mirrors

Michael J. Shepherd,* Richard G. Cobb,† Anthony N. Palazotto,‡ and William P. Baker§
Air Force Institute of Technology, Wright–Patterson Air Force Base, Ohio 45433

DOI: 10.2514/1.33344

Active lightweight continuous mirrors such as deformable membrane mirrors provide the capability to form conjugate surfaces that are effective for removing atmospheric distortions of an incoming wave front. Ongoing research for membrane mirrors for space telescopes has highlighted the need for a simple transformation between Zernike basis functions used by the optical community and the physically realizable dynamic modes of a membrane telescope more commonly recognized by the structural engineer. Perfect surface control would have authority to command both Zernike and vibration-mode shapes. However, the basis functions are incongruent in terms of boundary conditions. The research herein attempts to provide a simple tool for reconciling this otherwise imposing incompatibility. This paper provides design criteria for establishing achievable surface-deflection performance inside of a clear-aperture region for a preselected number of desired Zernike polynomials and a number of retained quasi-statically-actuated vibration-mode shapes. The methodology, coined the “modal transformation method” by the authors, is contrasted with a direct projection method in an applied example performed on a MSC.Nastran nonlinear finite element model of a piezoelectric-actuated deformable membrane mirror.

Nomenclature

A_n^m	= Zernike normalization constant
A_N^m	= Zernike transformation matrix
$a_i^{(m,n)}$	= Zernike transformation-matrix coefficient
B_n^m	= vibration-mode normalization constant
B_N^m	= vibration modal transformation matrix
$b_i^{(m,n)}$	= vibration transformation-matrix coefficient
$c_n^{(i)}$	= projection theorem coefficient
d_{31}	= piezoelectric coefficient
e	= Napier’s constant, ≈ 2.718
$F_i(r, \theta)$	= indicator function representing the area of the i th electrode
h	= distance from the neutral axis
J_m	= m th-order Bessel function of the first kind
M	= piezoelectric forcing
\tilde{m}	= azimuthal frequency
\tilde{N}	= weighting matrix
n	= radial degree
R	= radius
R_n^m	= Zernike radial polynomial
r	= radial coordinate
\hat{r}	= normalized radial coefficient
S_N^m	= scaling matrix
T	= edge tension
t	= piezoelectric-layer thickness
V_n	= applied voltage function
W_{C_m}	= vector of vibration modes of frequency m with cosine angular dependence
W_o	= vector of asymmetric vibration modes

W_{S_m}	= vector of vibration modes of frequency m with sine angular dependence
$W_n^m(r, \theta)_C$	= vibration-mode shape with cosine behavior
$W_n^m(r, \theta)_S$	= vibration-mode shape with sine behavior
$W_n^m(r, \theta)_0$	= vibration-mode shape with axisymmetric behavior
w	= out-of-plane surface displacement
Z_{C_m}	= vector of Zernike modes of frequency m with cosine angular dependence
Z_i	= i th Zernike polynomial
Z_o	= vector of asymmetric Zernike modes
Z_{S_m}	= vector of Zernike modes of frequency m with sine angular dependence
$\alpha_i^{(m,n)}$	= intermediary vibration transformation-matrix coefficient
β_{mn}	= n th zero of the m th-order Bessel function
δ_{ij}	= Kronecker delta
ϵ	= error bound
θ	= azimuthal coordinate, rad
κ	= index of the truncated polynomial
λ	= separation constant
ν	= Poisson’s ratio
ρ	= mass density per surface area
ω	= natural frequency

I. Introduction

THE active surface shape control of deformable membrane mirrors is of interest to researchers developing the next generation of spaceborne telescopes. Whether used for terrestrial observation or celestial discovery, the performance of spaceborne telescopes is ultimately governed by the size of their light-gathering aperture. Future telescopes are envisioned with apertures tens of meters in diameter. This leap in scale must overcome the packaging limitations that have heretofore restricted today’s meter-class mirror diameters. These large telescopes must be designed and fabricated to allow for collapsed packaging that may be then unfurled once in orbit.

This class of collapsible large-scale space-based reflectors was outlined by Agnes and Dooley [1] and is proposed by NASA for use in the L2 observatory [2]. For these conceptual designs, the mirror retains its shape primarily by acting as an edge-tensioned membrane with embedded active elements for fine-surface shape control. Other strategies for prestraining a mirror include using an intrinsic tension field [3,4], pressurizing a lenticular vessel with membrane surfaces

Received 9 July 2007; revision received 11 April 2008; accepted for publication 15 April 2008. This material is declared a work of the U.S. Government and is not subject to copyright protection in the United States. Copies of this paper may be made for personal or internal use, on condition that the copier pay the \$10.00 per-copy fee to the Copyright Clearance Center, Inc., 222 Rosewood Drive, Danvers, MA 01923; include the code 0731-5090/09 \$10.00 in correspondence with the CCC.

*Lt. Col., U.S. Air Force; Adjunct Professor; Director of Technical Support, U.S. Air Force Test Pilot School, Edwards Air Force Base, CA. Member AIAA.

†Assistant Professor, Department of Aeronautics and Astronautics. Senior Member AIAA.

‡Professor, Department of Aeronautics and Astronautics. Fellow AIAA.

§Associate Professor, Department of Mathematics and Statistics.

[5–7], or combining the pressurized lenticular with radial-tensioned cables for figure control [8]. Initial proof-of-concept efforts at the Air Force Institute of Technology have concentrated on the fabrication and design of small-scale flat demonstrator mirrors, such as those pictured in Fig. 1.

Although the research provided herein was initially conducted to correct surface errors on large-scale spaceborne membrane mirrors, the control concepts used on the demonstrator mirror could universally be applied on any two-dimensional membrane mirror in an optics application. For any circular aperture, the two-dimensional surface corrections these mirrors must impart on an incoming wave front are most often described by a truncated set of Zernike-polynomial basis functions. Simultaneously, there exists a requirement in active lightweight membrane mirrors to resist the effects of vibration disturbances that could build at resonance and adversely distort the membrane surface. The spatial content of this motion is typically described by a finite set of Bessel-function-based vibration modes below a frequency of interest. To control the vibration modes it is advantageous to actuate the same shapes for the purpose of attenuation.

The modal transformation method presented herein provides a simple algebraic transformation that is unique to this class of problem. A significant advantage of this technique is that it addresses the problem of the incompatible edge condition between the Zernike-polynomial basis set and the fixed-edge condition of the membrane mirror by introducing a definitive term for the usable region of the membrane mirror.

II. Background

Active quasi-static shape control of circular apertures to produce Zernike-polynomial surfaces has been explored by a myriad of researchers. A review of the Zernike-polynomials basis set follows, but for now it suffices to say that Zernike polynomials will always have some displacement at their boundary, and the tensioned-membrane structures envisioned in this application are characterized by a fixed, nondisplacing, boundary. This incompatible boundary condition has led to a series of case studies in which performance was either overly optimistic in the case in which the boundary condition was ignored or artificially limited when the boundary condition negatively influenced the results.

Wang and Hadaegh [9] presented the problem of surface control for a circular deformable mirror in terms of any orthogonal basis set and provided an example in which a circular membrane mirror is controlled by electrostatic actuators to form the axisymmetric Zernike shapes. The research did not account for a constrained boundary and thus promised a result not realizable with a fixed-frame membrane mirror.

Forming Zernike shapes on electrostatic membrane mirrors (mirrors that are forced by electrostatic attraction between electrode pairs on the mirror and a backing plate) has long relied on iterative techniques and calibration curves. Claflin and Bareket [10] published

a basic least-squares fitting technique in 1986. Tokovinin et al. [11] presented the experimental results of a 50-mm 79-actuator electrostatic membrane mirror for which only the interior 35-mm “pupil” was actuated. The solution methodology of using numerical solutions to Poisson’s equation (the governing equation for membrane structures) with an unused transition zone between the measured interior area and the fixed membrane boundary showed the difficulty of using membrane mirrors to make Zernike shapes.

Flint and Denoyer [12] showed the feasibility of using in-plane-actuated mirrors to produce Zernike-polynomial mode shapes again on some interior region of a circular membrane. Their results showed the promise of the mirror type but were tempered by difficulties in computing influence functions due to numerical instabilities. Another observation of Flint and Denoyer’s work was that the Zernike-mode shapes were best observed when the interior 80–90% of the circular aperture was used for Zernike formation, and it highlighted the need for resolving the incompatibility of a Zernike surface with a membrane mirror. A similar membrane construction was explored by Rogers and Agnes [13]. By exploring only axisymmetric cases and not attempting to individually actuate Zernike-mode shapes, the cases under study did not reveal the nature of the incompatible boundary conditions.

The purpose of this paper is to cast the surface control problem to one in which the desired surface shape expressed in terms of Zernike polynomials inside of a region that we will define as the “clear aperture” can be achieved by the use of statically actuated vibration-mode shapes (the Bessel-based functions that satisfy the fixed-edge condition). The terminology *clear aperture* was used in a figure in a 1977 work by Pearson and Hansen [14] to describe an area on a deformable mirror from which data were taken and thus is similar to our purpose. A notional mirror is displayed in Fig. 2, which shows a Zernike tilt surface deflection achieved inside of a clear-aperture region.

To achieve static surface control, an analytical formulation designated by the authors as the modal transformation method is developed. A brief outline of the technical development in the paper follows:

Section III reviews the two commonly used basis sets to describe a circular aperture. The Zernike-polynomial basis set is favored by the optics community, and the Bessel-based vibration-mode set is applied to physical solutions of the partial differential equation modeling a tensioned membrane. The fundamental premise of the modal transformation method is to cast the problem of obtaining Zernike polynomials by using a linear combination of statically actuated Bessel-function-based vibration modes.

Section IV develops the transformation matrices for the radial behavior of the Zernike polynomials and approximated vibration modes in terms of an intermediary radial polynomial basis. The vibration modes must be approximated due to the infinite series representation of the Bessel functions; thus, convergence and associated truncation error for a maximum radial polynomial degree is investigated.

Section V outlines the modal transformation method. The method is inspired by the projection theorem and an existing analytical relationship between the Zernike polynomials and the Bessel functions. The transformation matrices of the preceding section are combined and scaled to allow for increased accuracy inside of an interior clear-aperture region. Numerical issues with the transformation matrices are explored.

Section VI shows the significance of the methodology. The results are applied to a deformable membrane mirror modeled with finite elements in MSC.Nastran that uses piezoelectric in-plane actuation to create changes in surface curvature. Advantages in ease of

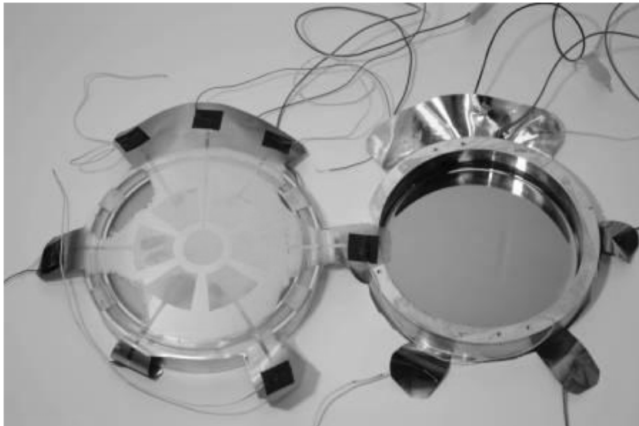


Fig. 1 Five-inch membrane mirrors at AFIT.

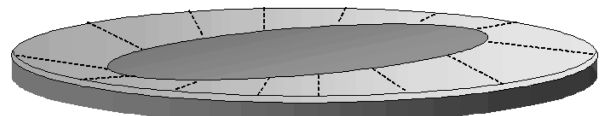


Fig. 2 Notional mirror with a surface tilt deflection achieved inside of the clear aperture.

numerical computation of actuator gains, combined with theoretical a priori knowledge of expected error, are shown. Specifically, surface error is shown to be a function of design criteria such as mirror diameter, fineness of actuation grid, diameter of the clear-aperture region, and order of the Zernike mode achieved. These results directly enable design trade studies in terms of acceptable surface-error values.

III. Basis Sets for Circular Apertures

Deformable membrane mirrors are employed to form conjugate surfaces to remove distortions in an incoming wave front. For a flat circular aperture, the two-dimensional surface corrections are most often provided in the form of a scaled truncated set of the Zernike-polynomial basis functions. Simultaneously, there exists a requirement in lightweight membrane mirrors to actively resist dynamic effects that could build at resonance and adversely distort the membrane surface, which are typically modeled as a finite set of Bessel-function-based vibration modes below a frequency of interest. However, Zernike modes and vibration modes fundamentally differ in that a Zernike mode always has a vertical displacement at the edge, whereas the vibration mode does not displace vertically from the mirror frame (edge). Pictorial representations for Zernike and vibration modes are provided in Tables 1 and 2, respectively.

Inspired by the understanding of the pictorial representation of the two basis functions, we begin this section with a discussion of the mathematical properties and notation associated with the Zernike polynomial, and a matrix representation of the Zernike polynomials is derived. The vibration modes are then reviewed for a circular membrane, and an analogous matrix representation is created, with the primary difference being that the matrix was formed from a truncated subset of the infinite series representation. Next, a direct Zernike-to-vibration-mode transformation is created, both in integral form and then using radial coordinates. Definition of a clear-aperture

region (an interior region on a circular aperture in which Zernike-mode shapes will be formed) is then proposed and a series of examples follow.

A. Definition of the Zernike Polynomial

The optics community has used the modified set of Zernike polynomials, as first defined by Noll [15], to describe aberrations in an incoming wave front. The Zernike polynomials Z_i are orthogonal over the interior of the domain of circular aperture of unit radius through the relationship

$$\int_0^{2\pi} \int_0^1 \frac{1}{\pi} Z_i Z_j r dr d\theta = \delta_{ij} \quad (1)$$

where δ_{ij} is the Kronecker delta. The polynomials Z_i are defined as

$$\left. \begin{aligned} Z_{\text{even}j} &= A_n^m R_n^m \cos m\theta \\ Z_{\text{odd}j} &= A_n^m R_n^m \sin m\theta \end{aligned} \right\}, \quad m \neq 0 \quad (2)$$

$$Z_j = A_n^m R_n^m, \quad m = 0 \quad (3)$$

with A_n^m is the normalization constant, and R_n^m is the radial polynomial for azimuthal frequency m and radial degree n . The radial polynomial R_n^m is defined as

$$R_n^m(r) = \sum_{s=0}^{(n-m)/2} \frac{(-1)^s (n-s)!}{s!(m-s)!(n-m-s)!} r^{n-2s} \quad (4)$$

where the values of the azimuthal frequency m are less than or equal to the radial degree n ($m \leq n$) and $n-m$ is even. The radial polynomials are presented in Table 3 [15].

The normalization constants A_n^m are defined to maintain the orthonormal relationship with respect to the weighted function in Eq. (1):

Table 1 Pictorial representation of Zernike-mode shapes





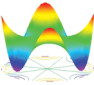




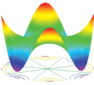
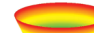



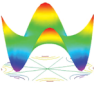




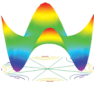




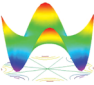
	$m = 0$	$m = 1$	$m = 2$	$m = 3$	$m = 4$
$n = 0$	Piston 				
$n = 1$		Tilt 			
$n = 2$	Defocus 		Astigmatism 		
$n = 3$		Coma 			
$n = 4$	Spherical 				

Table 2 Pictorial representation of vibration-mode shapes with normalized natural frequency ω_{mn}


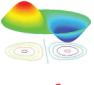
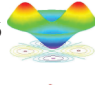
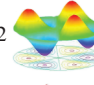
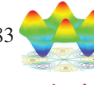
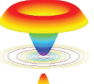
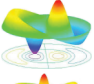
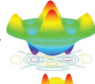
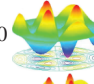
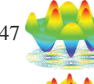
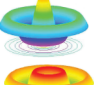
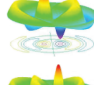
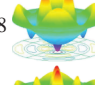
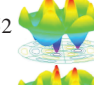
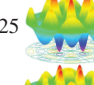
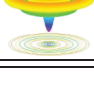
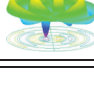
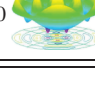
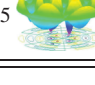
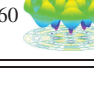
	$m = 0$	$m = 1$	$m = 2$	$m = 3$	$m = 4$
$n = 1$	2.4048 	3.8317 	5.1356 	6.3802 	7.5883 
$n = 2$	5.5201 	7.0156 	8.4172 	9.7610 	11.0647 
$n = 3$	8.6537 	10.1735 	11.6198 	13.0152 	14.3725 
$n = 4$	11.7915 	13.3237 	14.7960 	16.2235 	17.6160 

Table 3 Radial polynomials R_n^m

	$m = 0$	$m = 1$	$m = 2$	$m = 3$	$m = 4$	$m = 5$
$n = 0$	1	—	—	—	—	—
$n = 1$	$2r^2 - 1$	r	r^2	—	—	—
$n = 2$	—	$3r^3 - 2r$	—	—	—	—
$n = 3$	$6r^4 - 6r^2 + 1$	—	$4r^4 - 3r^2$	r^3	—	—
$n = 4$	—	$10r^5 - 12r^3 + 3r$	—	—	r^4	—
$n = 5$	$20r^6 - 30r^4 + 12r^2 - 1$	—	$15r^6 - 20r^4 + 6r^2$	$5r^5 - 4r^3$	—	r^5
$n = 6$	—	$35r^7 - 60r^5 + 30r^3 - 4r$	—	$21r^7 - 30r^5 + 10r^3$	$6r^6 - 5r^4$	—
$n = 7$	$70r^8 - 140r^6 + 90r^4 - 20r^2 + 1$	—	$56r^8 - 105r^6 + 60r^4 - 10r^2$	$21r^7 - 30r^5 + 10r^3$	$28r^8 - 42r^6 + 15r^4$	$7r^7 - 6r^5$
$n = 8$	—	$126r^9 - 280r^7 + 210r^5 - 60r^3 + 5r$	—	$84r^9 - 168r^7 + 105r^5 - 20r^3$	—	$36r^9 - 56r^7 + 21r^5$
$n = 9$	—	—	—	—	—	—

$$A_n^m = \sqrt{2(n+1)}, \quad m \neq 0 \quad (5)$$

$$A_n^m = \sqrt{(n+1)}, \quad m = 0 \quad (6)$$

The normalization constants are the coefficients of the terms in Table 4. The Zernike polynomials may be alternately referred to as Zernike-mode shapes, recognizing that for the purpose of this document, the Zernike-mode shapes represent desired surface deflections.

B. Definition of Vibration Modes

Although the Zernike-mode shapes represent the commanded desired static shapes that we wish the circular aperture to obtain, the dynamic motion of the circular membrane is governed by vibration-mode shapes. The vibration-mode shapes represent the eigenfunctions associated with the natural modes of the system. The vibration-mode shapes of the uniform circular membrane of radius ($0 \leq r \leq R$), edge tension T , mass density per surface area ρ , and edge (boundary) condition $w(R, \theta, t) = 0$ may be found by solving the partial differential equation

$$T\nabla^2 w(r, \theta, t) - \rho \ddot{w}(r, \theta, t) = 0 \quad (7)$$

through a separation of variables in which the separation constant $\lambda = \omega^2$ is such that the spatial mode equation may be written as

$$\nabla^2 W(r, \theta) + \beta^2 W(r, \theta) = 0, \quad \beta = \frac{\rho \omega^2}{T} \quad (8)$$

Using the separation-of-variables technique to simplify the partial differential equation for the case of a pinned boundary [$W(R, \theta) = 0$], the static mode shapes are obtained. The derivation may be found in a structural dynamics textbook, such as the text by Meirovitch [16]. The mode shapes are

$$W_n^m(r, \theta)_C = B_n^m J_m(\beta_{mn} r) \cos m\theta, \quad m, n = 1, 2, \dots \quad (9)$$

$$W_n^m(r, \theta)_S = B_n^m J_m(\beta_{mn} r) \sin m\theta, \quad m, n = 1, 2, \dots \quad (10)$$

$$W_n^0(r, \theta) = B_n^0 J_0(\beta_{0n} r), \quad n = 1, 2, \dots \quad (11)$$

where

$$B_n^m = \frac{\sqrt{2}}{\sqrt{\pi \rho R (J_{m+1}(\beta_{mn} R))}}, \quad m = 1, 2, \dots \quad (12)$$

$$B_n^m = \frac{1}{\sqrt{\pi \rho R (J_1(\beta_{mn} R))}}, \quad m = 0 \quad (13)$$

The indices m and n represent the azimuthal frequency and radial frequency, respectively. The radial frequency is actually the n th zero of the associated m th-order Bessel function and may be thought of as the number of times the Bessel function crosses the radial axis between the center of the membrane and the boundary.[†] The vibration modes of the circular membrane are orthogonal through the relationship

$$\int_0^{2\pi} \int_0^R \rho W_{nl}^m W_{qj}^p r dr d\theta = \delta_{lj} \delta_{mp} \delta_{nq} \quad (14)$$

[†]The vibration-mode shape always satisfies the boundary condition of zero displacement at the boundary through the condition $J_m(\beta_{mn} R) = 0$.

Table 4 Zernike polynomials using Noll's ordering [15], in which R_n^m are defined as in Table 3

	$m = 0$	$m = 1$	$m = 2$	$m = 3$	$m = 4$
$n = 0$	$Z_1 = R_0^0$ Piston	—	—	—	—
$n = 1$	—	$Z_2 = 2R_1^1 \cos \theta$ $Z_3 = 2R_1^1 \sin \theta$ Tilt	—	—	—
$n = 2$	$Z_4 = \sqrt{3}R_2^0$ Defocus	—	$Z_5 = \sqrt{6}R_2^2 \sin 2\theta$ $Z_6 = \sqrt{6}R_2^2 \cos 2\theta$ Astigmatism	—	—
$n = 3$	—	$Z_7 = \sqrt{8}R_3^1 \sin \theta$ $Z_8 = \sqrt{8}R_3^1 \cos \theta$ Coma	—	$Z_9 = \sqrt{8}R_3^3 \sin 3\theta$ $Z_{10} = \sqrt{8}R_3^3 \cos 3\theta$	—
$n = 4$	$Z_{11} = \sqrt{5}R_4^0$ Spherical	—	$Z_{12} = \sqrt{10}R_4^2 \cos 2\theta$ $Z_{13} = \sqrt{10}R_4^2 \sin 2\theta$	—	$Z_{14} = \sqrt{10}R_4^4 \cos 4\theta$ $Z_{15} = \sqrt{10}R_4^4 \sin 4\theta$
$n = 5$	—	$Z_{16} = \sqrt{12}R_5^1 \cos \theta$ $Z_{17} = \sqrt{12}R_5^1 \sin \theta$	—	$Z_{18} = \sqrt{12}R_5^3 \cos 3\theta$ $Z_{19} = \sqrt{12}R_5^3 \sin 3\theta$	—

IV. Matrix Representations of Modal Transformation

In this section, we formulate a matrix representation of the radial Zernike-polynomial and vibration-mode basis sets (note that the azimuthal, or angular, behavior is identical for both basis sets). To do that, the radial behavior of each basis set is cast in terms of an intermediary polynomial basis. Because the Bessel-function component of the vibration modes consists of an infinite series in the intermediary basis, the resulting modes are therefore an approximation to the vibration modes, subject to truncation error.

A. Zernike Transformation Matrix for a Given Azimuthal Frequency

Equation (3) terms $A_m^n R_n^m$ may be written in a summation form in which the coefficients are as given in Table 3. For a given azimuthal frequency m , the summation will have the form in which each row represents the maximum radial degree of the polynomial:

$$\begin{aligned}
 A_n^m R_n^m &= \sum_{k=0}^N \left(a_{2k}^{(m,n)} \right) r^{2k} r^m \\
 &= \left(a_0^{(m,n)} + a_2^{(m,n)} r^2 + \dots + a_N^{(m,n)} r^{2N} \right) r^m \\
 &= \begin{bmatrix} a_0^{(m,n)} \\ a_2^{(m,n)} \\ \vdots \\ a_N^{(m,n)} \end{bmatrix}^T \begin{bmatrix} 1 \\ r^2 \\ \vdots \\ r^{2N} \end{bmatrix} r^m
 \end{aligned} \tag{15}$$

Furthermore, we can write a series of equations for a given azimuthal frequency m that encompass all radial degrees from m to a maximum degree of n such that

$$\begin{aligned}
 &\begin{bmatrix} A_m^m R_m^m \\ A_{m+2}^{m+2} R_{m+2}^{m+2} \\ \vdots \\ A_{m+2N}^{m+2N} R_{m+2N}^{m+2N} \end{bmatrix} \\
 &= \begin{bmatrix} a_0^{(m,m)} & & & \\ a_0^{(m,m+2)} & a_2^{(m,m+2)} & & \\ & \vdots & \ddots & \\ a_0^{(m,m+2N)} & a_2^{(m,m+2N)} & & a_{2N}^{(m,m+2N)} \end{bmatrix} \begin{bmatrix} 1 \\ r^2 \\ \vdots \\ r^{2N} \end{bmatrix} r^m
 \end{aligned} \tag{16}$$

The Zernike transformation matrix A_N^m may therefore be defined as the lower diagonal transformation matrix of size $N + 1 \times N + 1$ for an azimuthal frequency m with a maximum polynomial degree $2N + m$ from above. A_N^m is here defined as

$$A_N^m \equiv \begin{bmatrix} a_0^{(m,m)} & & & \\ a_0^{(m,m+2)} & a_2^{(m,m+2)} & & \\ & \vdots & \ddots & \\ a_0^{(m,m+2N)} & a_2^{(m,m+2N)} & & a_{2N}^{(m,m+2N)} \end{bmatrix}$$

B. Vibration-Mode Transformation Matrix for a Given Azimuthal Frequency

It is our desire to expand the vibration-mode shapes from Sec. III.B. We will accomplish this by creating a vibration-mode transformation matrix for a given azimuthal frequency. To obtain our transformation matrix, we begin by writing the series representation of the Bessel functions in terms of bookkeeping coefficients $\alpha_{2k}^{(m,n)}$:

$$\begin{aligned}
 J_m(\beta_{mn} r) &= \left(\frac{1}{2} \beta_{mn} r \right)^m \sum_{k=0}^{\infty} \frac{(-1)^k \left(\frac{1}{2} \beta_{mn} r \right)^{2k}}{(k+m)! k!} \\
 &= \sum_{k=0}^{\infty} \alpha_{2k}^{(m,n)} r^{2k+m} = \left(\alpha_0^{(m,n)} + \alpha_2^{(m,n)} r^2 + \dots \right) r^m \\
 &= \begin{bmatrix} \alpha_0^{(m,n)} & \alpha_2^{(m,n)} & \dots \end{bmatrix} \begin{bmatrix} 1 \\ r^2 \\ \vdots \end{bmatrix} r^m
 \end{aligned} \tag{17}$$

Next, we apply the vibration-mode-shape normalization coefficients from Eqs. (12) and (13) such that $b_{2k}^{(m,n)} = B_n^m \alpha_{2k}^{(m,n)}$ and arrive at

$$B_n^m J_m(\beta_{mn} r) = \sum_{k=0}^{\infty} (b_{2k}^{(m,n)}) r^{2k} r^m = \begin{bmatrix} b_0^{(m,n)} & b_2^{(m,n)} & \dots \end{bmatrix} \begin{bmatrix} 1 \\ r^2 \\ \vdots \end{bmatrix} r^m \tag{18}$$

We desire a transformation matrix analogous to Eq. (17) for a given azimuthal frequency m . Therefore, we construct a series of equations from Eq. (18) such that

$$\begin{bmatrix} B_1^m J_m(\beta_{m1} r) \\ B_2^m J_m(\beta_{m2} r) \\ \vdots \end{bmatrix} = \begin{bmatrix} b_0^{(m,1)} & b_2^{(m,1)} & \dots \\ b_0^{(m,2)} & b_2^{(m,2)} & \dots \\ \vdots & \vdots & \ddots \end{bmatrix} \begin{bmatrix} 1 \\ r^2 \\ \vdots \end{bmatrix} r^m \tag{19}$$

We then construct a series of $N + 1$ equations and truncate the approximations to a maximum radial polynomial degree of $2N + m$. The equations are

$$\begin{pmatrix} B_1^m J_m(\beta_{m1} r) \\ B_2^m J_m(\beta_{m2} r) \\ \vdots \\ B_{N+1}^m J_m(\beta_{m(2N)} r) \end{pmatrix} \approx \begin{bmatrix} b_0^{(m,1)} & b_2^{(m,1)} & \dots & b_{2N}^{(m,1)} \\ b_0^{(m,2)} & b_2^{(m,2)} & \dots & b_{2N}^{(m,2)} \\ \vdots & \vdots & \ddots & \vdots \\ b_0^{(m,N+1)} & b_2^{(m,N+1)} & \dots & b_{2N}^{(m,N+1)} \end{bmatrix} \begin{pmatrix} 1 \\ r^2 \\ \vdots \\ r^{2N} \end{pmatrix} r^m \quad (20)$$

From Eq. (20), we define our $N + 1 \times N + 1$ vibration modal transformation matrix \mathbf{B}_N^m as follows:

$$\mathbf{B}_N^m \equiv \begin{bmatrix} b_0^{(m,1)} & b_2^{(m,1)} & \dots & b_{2N}^{(m,1)} \\ b_0^{(m,2)} & b_2^{(m,2)} & \dots & b_{2N}^{(m,2)} \\ \vdots & \vdots & \ddots & \vdots \\ b_0^{(m,N+1)} & b_2^{(m,N+1)} & \dots & b_{2N}^{(m,N+1)} \end{bmatrix} \quad (21)$$

The invertibility of the matrix \mathbf{B}_N^m is discussed in Sec. V.D. Furthermore, the Bessel terms in Eq. (20) will only be correctly represented to the precision shown in the next section.

C. Convergence of the Bessel (Alternating) Series and Associated Truncation Error

Our goal is to be able to transform information of the surface deformation from our Zernike subspace to vibration modal coordinates and vice versa. To write the Zernike polynomials in terms of the modal coordinates, we will need a finite expression of the Bessel functions in our intermediate coordinate system of radius and azimuthal angles.

By definition, the Bessel functions may be written as the series [17]

$$J_m(\beta_{mn} r) = \left(\frac{1}{2}\beta_{mn} r\right)^m \sum_{k=0}^{\infty} \frac{(-1)^k \left(\frac{1}{2}\beta_{mn} r\right)^{2k}}{(k+m)!k!} \quad (22)$$

For the symmetric modes, $m = 0$ and Eq. (22) may be reduced to

$$J_0(\beta_{0n} r) = \sum_{k=0}^{\infty} \frac{(-1)^k \left(\frac{1}{2}\beta_{0n} r\right)^{2k}}{k!^2} \quad (23)$$

For instance, the first zero of $J_0(\beta R) = 0$ is $\beta_{01} = 2.4048/R$ and the infinite summation in which $\tilde{r} \equiv r/R$ (representing the normalized mirror radius):

$$J_0(2.4048\tilde{r}) = 1 - 1.4458\tilde{r}^2 + 0.52258\tilde{r}^4 + \mathcal{O}(\tilde{r}^6) \quad (24)$$

Returning to the general case of any nonnegative integer m , to accomplish our desired transformation, we must approximate the Bessel functions by a truncated series. We note here that in the future sections we will directly relate the Zernike modes with the Bessel-based vibration modes. The two basis sets have exactly the same azimuthal behavior. Thus, it is the error in the radial terms that will contribute to the overall error in the relationship. To this end, the degree of truncation is estimated to ensure accuracy to within some approximation tolerance ϵ .

Begin by defining

$$B_m^\kappa(\beta_{mn} r) \equiv \sum_{k=0}^{\kappa-1} \frac{(-1)^k \left(\frac{1}{2}\beta_{mn} r\right)^{2k+m}}{(k+m)!k!} \quad (25)$$

where, again, $\tilde{r} \equiv r/R$. From this point, we will drop the tilde, realizing that our r is a normalized value. Note this is simply the first κ terms of the Bessel series.

Next, choose κ such that

$$|J_m(\beta_{mn} r) - B_m^\kappa(\beta_{mn} r)| < \epsilon \quad (26)$$

Because the Bessel function is an alternating series, the error in truncating the series is no worse than the first term neglected. The error of Eq. (26) is therefore bounded as

$$|J_m(\beta_{mn} r) - B_m^\kappa(\beta_{mn} r)| \leq \frac{\left(\frac{1}{2}\beta_{mn} r\right)^{2\kappa+m}}{(\kappa+m)! \kappa!} \quad (27)$$

Further, because $m \geq 0$, we have

$$\frac{\left(\frac{1}{2}\beta_{mn} r\right)^{2\kappa+m}}{(\kappa+m)! \kappa!} < \frac{\left(\frac{1}{2}\beta_{mn} r\right)^{2\kappa+m}}{(\kappa!)^2} \quad (28)$$

For large values of κ , Stirling's formula may be used to simplify large values of the factorial expression $\kappa!$:

$$\kappa! \approx \kappa^\kappa e^{-\kappa} \sqrt{2\pi\kappa} \quad (29)$$

Applying Stirling's formula, the magnitude of the error becomes

$$\frac{e^{2\kappa} \left(\frac{1}{2}\beta_{mn} r\right)^{2\kappa+m}}{2\pi\kappa^{2\kappa+1}} < \epsilon \quad (30)$$

Upon further simplification, our error-bound formula is

$$\frac{\left(\frac{1}{2}\beta_{mn} r\right)^m}{2\pi\kappa} \left(\frac{e\beta_{mn} r}{2\kappa}\right)^{2\kappa} < \epsilon \quad (31)$$

This truncation error represents an error bound on the radial portion of the truncated modes. In future constructs when approximating Bessel functions, enough terms should be chosen so that this error is negligible.

V. Modal Transformation Method for Circular Apertures

In this section, a method is developed that allows Zernike surfaces to be projected on an interior region of a circular aperture by a linear combination of Bessel-based vibration-mode shapes. In short, by comprising a desired optical surface in terms of physically realizable mode shapes, steady-state surface control should be readily achievable.

A. Projection of the Zernike Modes onto the Vibration Modes

The Zernike polynomials of Sec. III.A are related to the Bessel function of the first kind by the formula presented by Noll [15]:

$$R_n^m(r) = 2\pi(-1)^{(n-m)/2} \int_0^{\infty} J_{n+1}(2\pi\xi) J_m(2\pi\xi r) d\xi \quad (32)$$

Therefore, we expect it is reasonable to express Zernike-mode shapes in terms of vibration-mode shapes. To do so, an approach was developed based upon the orthogonal properties of the two basis sets and the projection theorem.

B. Existing Analytical Relationship

To define a Zernike mode in terms of a vibration mode, first consider the case of the axisymmetric modes. We desire

$$Z_i = \sum_{n=0}^{\infty} c_n^{(i)} W_n^0 \quad (33)$$

Therefore, we may write (assuming both mode shapes have been normalized to the same unit radius) the coefficients based upon the projection theorem as

$$c_n^{(i)} = \frac{\int_0^{2\pi} \int_0^1 (1/\sqrt{\pi}) Z_i(r) W_n^0(r) r dr d\theta}{\int_0^{2\pi} \int_0^1 (W_n^0(r))^2 r dr d\theta} \quad (34)$$

noting that there is no dependence on θ such that the azimuthal integral term is replaced by the quantity 2π . The term $1/\sqrt{\pi}$ is required because Noll's [15] scheme as presented in Eq. (1) requires a linear weighting, which is equally distributed among the Zernike modes in our relationships. Further note that the vibration modes are already normalized; thus, Eq. (34) reduces to

$$c_n^{(i)} = 2\pi \int_0^1 \frac{1}{\sqrt{\pi}} Z_i(r) W_n^0(r) r dr \quad (35)$$

Substituting the results of mode-shape equations (11) and (13) with unit density (and $R = 1$) yields

$$c_n^{(i)} = \frac{2}{J_1(\beta_{0n})} \int_0^1 Z_i J_0(\beta_{0n} r) r dr \quad (36)$$

The approximation of the piston Zernike mode using a linear combination of the first 20 axisymmetric vibration-mode shapes from the projection theorem as developed in Eqs. (33–36) is presented in Fig. 3.

From this section, we make the following observations. In Fig. 3, even with a linear combination of 20 mode shapes, we observe nearly 20% error at a normalized radius of 0.9–1.0. Also, the representation is computationally intensive due to numeric integration. Thus, we seek a simpler solution in which integration is avoided and a bound on relative error may be forecast.

C. Zernike-to-Vibration-Mode Matrix Transformation

Although Eq. (33) allows the Zernike modes to be written in the form of integral equations, we may alternately apply the results of Secs. IV.A and IV.B to write an approximate modal transformation. Begin by defining a vector of Zernike and vibration modes for a given frequency for radial degrees up to $2N$. For simplicity, we define the axisymmetric case:

$$\mathbf{Z}_0 = \begin{Bmatrix} R_0^0 \\ \sqrt{3}R_2^0 \\ \vdots \\ \sqrt{2N+1}R_{2N}^0 \end{Bmatrix} = \mathbf{A}_N^0 \begin{Bmatrix} 1 \\ r^2 \\ \vdots \\ r^{2N} \end{Bmatrix} \quad (37)$$

and

$$\mathbf{W}_0 = \begin{Bmatrix} W_1^0 \\ W_2^0 \\ \vdots \\ W_{N+1}^0 \end{Bmatrix} = \mathbf{B}_N^0 \begin{Bmatrix} 1 \\ r^2 \\ \vdots \\ r^{2N} \end{Bmatrix} \quad (38)$$

Solve for radial vector $\{1, r^2, \dots, r^{2N}\}^T$ in Eq. (38),

$$\begin{Bmatrix} 1 \\ r^2 \\ \vdots \\ r^{2N} \end{Bmatrix} = (\mathbf{B}_N^0)^{-1} \mathbf{W}_0 \quad (39)$$

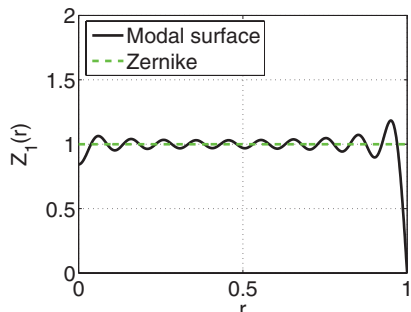


Fig. 3 Piston Zernike mode Z_1 approximated by a linear combination of the first 20 axisymmetric vibration-mode shapes.

and then substitute into Eq. (37) to yield the expression

$$\mathbf{Z}_0 = \mathbf{A}_N^0 (\mathbf{B}_N^0)^{-1} \mathbf{W}_0 \quad (40)$$

Through a similar manner, write the nonaxisymmetric equations:

$$\mathbf{Z}_{s_m} = \mathbf{A}_N^m (\mathbf{B}_N^m)^{-1} \mathbf{W}_{C_m} \quad (41)$$

$$\mathbf{Z}_{C_m} = \mathbf{A}_N^m (\mathbf{B}_N^m)^{-1} \mathbf{W}_{S_m} \quad (42)$$

where the modal vectors of length $N + 1$ are composed of modes of axisymmetric mode shapes (\mathbf{Z}_0 and \mathbf{W}_0), modes with cosine angular dependence of frequency m (\mathbf{Z}_{C_m} and \mathbf{W}_{C_m}), and modes with sine angular dependence of frequency m (\mathbf{Z}_{S_m} and \mathbf{W}_{S_m}).

D. Near Singularity of the Modal Transformation Matrix

The modal transformation matrix \mathbf{B}_N^m is most conveniently applied by defining it as a square matrix in Sec. IV.B, so that its inverse in Sec. V.C is unique. Nonsquare issues addressed with the pseudoinverse are not included herein.

The size of \mathbf{B}_N^m is determined by the number of (or highest degree) of vibration modes that the designer will be able to actuate: those modes are essentially dependent on the fineness of the actuator grid. The value of N should be large enough so that actuated modes are represented with a small-to-negligible truncation error, as derived in Eq. (31). However, the resulting \mathbf{B}_N^m is ill-conditioned and is not readily invertible for large values of N . A method for decomposing the matrix into a diagonal matrix $\tilde{\mathbf{N}}$ and remaining components $\tilde{\mathbf{B}}_N^m$ was applied to allow inversion on 32-bit processors for values of $N \leq 20$.

Begin by defining

$$\mathbf{B}_N^m \equiv \tilde{\mathbf{N}} \tilde{\mathbf{B}}_N^m \quad (43)$$

where the diagonal elements of $\tilde{\mathbf{N}}$ are defined as

$$\tilde{N}_{ii} = (\mathbf{B}_N^m)_{ii} \quad (44)$$

The remaining offdiagonal elements of $\tilde{\mathbf{N}}$ are zero. Thus constructed, much of the ill-conditioned nature of \mathbf{B}_N^m is shifted to $\tilde{\mathbf{N}}$, for which an analytical inverse readily exists.

As a simple example, for the case in which $N = 2$ and $m = 0$, ρ and R are normalized to 1, and the factor $1/\sqrt{\pi}$ is removed, the matrices are

$$\mathbf{B}_N^m = \begin{bmatrix} 1.0868 & -1.5712 & 0.5679 \\ -1.6581 & 12.6310 & -24.0552 \\ 2.0784 & -38.9115 & 182.1229 \end{bmatrix} \quad (45)$$

$$\tilde{\mathbf{N}} = \begin{bmatrix} 1.0868 & 0 & 0 \\ 0 & 12.6310 & 0 \\ 0 & 0 & 182.1229 \end{bmatrix} \quad (46)$$

$$\tilde{\mathbf{B}}_N^m = \begin{bmatrix} 1.0000 & -1.4458 & 0.5226 \\ -0.1313 & 1.0000 & -1.9045 \\ 0.0114 & -0.2137 & 1.0000 \end{bmatrix} \quad (47)$$

In this example, the original condition number of \mathbf{B}_N^m is reduced from 240.9 to 21.3 and the condition number of $\tilde{\mathbf{N}}$ is 167.5831, of little impact due to the ease of inverting $\tilde{\mathbf{N}}$ analytically, allowing $(\mathbf{B}_N^m)^{-1} = (\tilde{\mathbf{N}})^{-1} (\tilde{\mathbf{B}}_N^m)^{-1}$.

E. Defining a Clear-Aperture Control Region

To this point, every effort made focused on projecting a Zernike space onto a Bessel-based vibration-mode space. A valiant effort, yet one that will prove frustrating due to the incompatibility of the boundary conditions for these competing basis sets. To avoid this

inherent difficulty, it is proposed to define a clear-aperture region as a subspace of the Bessel-based vibration-mode space. Simply stated, the clear-aperture region will be a circular region with some radius $a < R$, as was first introduced in Fig. 2. Defining the scaled variable $\hat{r} = r/a$ for the Zernike polynomials in this subspace and noting that on the clear-aperture boundary $\hat{r} = 1$, we relate the polynomial vector $\{1, \hat{r}^2, \dots, \hat{r}^{2N}\}$ to the radial vector $\{1, r^2, \dots, r^{2N}\}$ with the diagonal matrix S_N^m . The matrix S_N^m is

$$S_N^m = \frac{1}{a^m} \begin{bmatrix} 1 & & & \\ & \frac{1}{a^2} & & \\ & & \ddots & \\ & & & \frac{1}{a^{2N}} \end{bmatrix} \quad (48)$$

such that

$$\begin{Bmatrix} 1 \\ \hat{r}^2 \\ \vdots \\ \hat{r}^{2N} \end{Bmatrix} \hat{r}^m = [S] \begin{Bmatrix} 1 \\ r^2 \\ \vdots \\ r^{2N} \end{Bmatrix} r^m \quad (49)$$

Again, as in previous sections, the transformation matrix is for an azimuthal frequency m with a maximum polynomial degree $2N + m$. For Zernike shape control of the clear-aperture region, the governing equations (40–42) scale to become

$$Z_0 = A_N^0 S_N^0 (B_N^0)^{-1} W_0 \quad (50)$$

$$Z_{S_m} = A_N^m S_N^m (B_N^m)^{-1} W_{C_m} \quad (51)$$

$$Z_{C_m} = A_N^m S_N^m (B_N^m)^{-1} W_{S_m} \quad (52)$$

F. Application of the Modal Transformation Method

With the underlying theory thus provided, a series of specific application of the modal transformation method for circular apertures is presented to show the applicable design criteria for deformable mirrors.

To begin, the method is compared with the projection theorem used in Sec. V.A. In Fig. 4, the radial behavior of a surface composed of the first 20 axisymmetric vibration-mode shapes is constructed to approximate the axisymmetric defocus Zernike mode, $Z_4 = \sqrt{3}(2r^2 - 1)$, over the entire surface (effectively, the clear aperture as previously presented is set to its maximum value of 1). In Fig. 4a, the representation is constructed using coefficients from the projection theorem, and in Fig. 4b, the coefficients were generated using the modal transformation method for $N = 20$. The error between the desired Zernike surface and the vibration modal representation was calculated using the discretized weighted Euclidean norm.

The discretized weighted Euclidean norm $\|\cdot\|_\Delta$ in cylindrical coordinates for radial grid spacing Δr and azimuthal spacing $\Delta\theta$ is

$$\|f - g\|_\Delta = \left(\Delta r \Delta\theta \sum_{i=1}^N r_i [f_i(r_i, 2\pi\theta_i) - g_i(r_i, 2\pi\theta_i)]^2 \right)^{\frac{1}{2}} \quad (53)$$

Assuming a circular domain with unit radius, this limit of the vector norm as the step size decreases yields the functional 2-norm:

$$\lim_{\Delta r, \Delta\theta \rightarrow 0} \|f - g\|_\Delta = \left(\int_0^{2\pi} \int_0^1 [f - g]^2 r dr d\theta \right)^{\frac{1}{2}} = \|f - g\|_2 \quad (54)$$

This result will give us a stable error term to use. Compare this norm to the familiar root-mean-square error, which does not account for the weighting factor r_i and does not readily account for differing grid spaces on orthogonal axes within the vectors themselves:

$$E_{\text{rms}} \equiv \frac{1}{N} \left(\sum_{i=1}^N [f_i - g_i]^2 \right)^{\frac{1}{2}} \quad (55)$$

Further note that in some cases presented, only radial error is reported, and thus the azimuthal terms (θ dependence) is not required.

With the clear aperture thus set to 1, the projection theorem results in the smaller error between the desired surface and its modal representation (in this example, the error values were 0.1753 versus 0.3585) and represents the best achievable performance for the linear system when mapped over the entire domain. However, the shape of the modal surface in Fig. 4a has evidence of distortion throughout its surface, and Fig. 4b shows significant distortion only at the outer edge, to meet the boundary condition.

Next, in Fig. 5, the clear aperture is adjusted to values less than one, and the defocus Zernike mode is constructed as in Fig. 4 using the modal transformation method. In Figs. 5a–5c, the radial behavior is plotted for clear apertures of 0.7, 0.8, and 0.9. It is quite apparent that for a clear aperture of 0.7, the deviation between the desired Zernike shape and the modal surface is indistinguishable at the scale shown.

With the clear aperture fixed at 0.7, another series of plots was constructed for Fig. 6, again using the modal transformation method for $N = 20$. This series of plots show not only the intuitive improvement in accuracy by increasing the number of modes to actuate the surface, but they also show that the improvement is from the interior of the clear aperture to a maximum difference at the boundary of the clear aperture.

Figure 7 captures the information from both Figs. 5 and 6 on a single graphic. The log of the surface error is shown to decrease with an increased number of actuated modes and a decreased clear aperture. For example, to get the level of error equal to 0.01, either set $N = 1$ and the clear aperture to 0.09 or set $N = 20$ and the clear aperture to 0.75.

For the structural engineer, these results may be transformed into design criteria for construction of a deformable mirror. Beginning with a desired optical surface-error budget and a desired radius of the aperture region, the engineer may choose to actuate a greater number of vibration modes or to reduce the clear aperture to achieve the

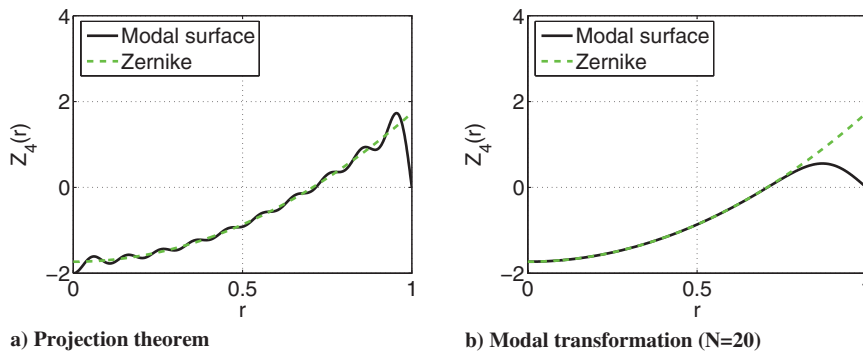


Fig. 4 Modal representations of the axisymmetric defocus Zernike.

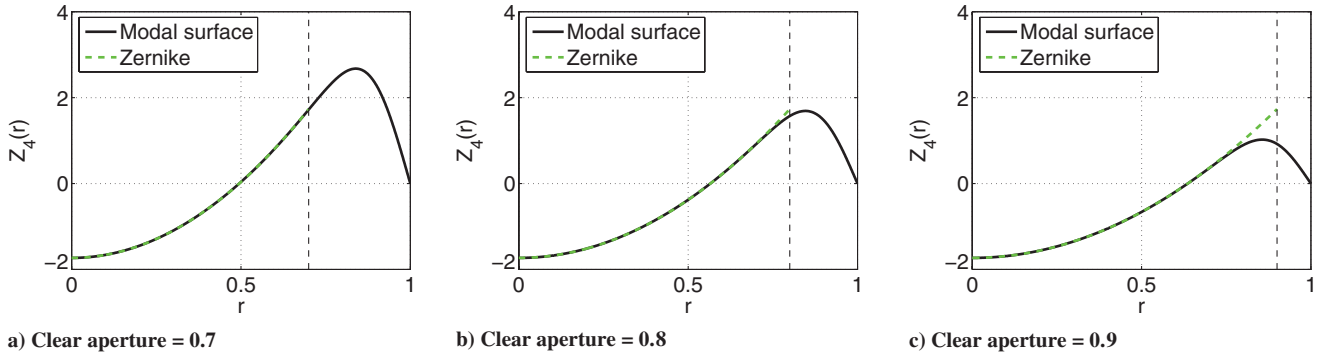


Fig. 5 Impact of the clear aperture on representation of the defocus Zernike by the first 20 axisymmetric vibration modes using the modal transformation for $N = 20$.

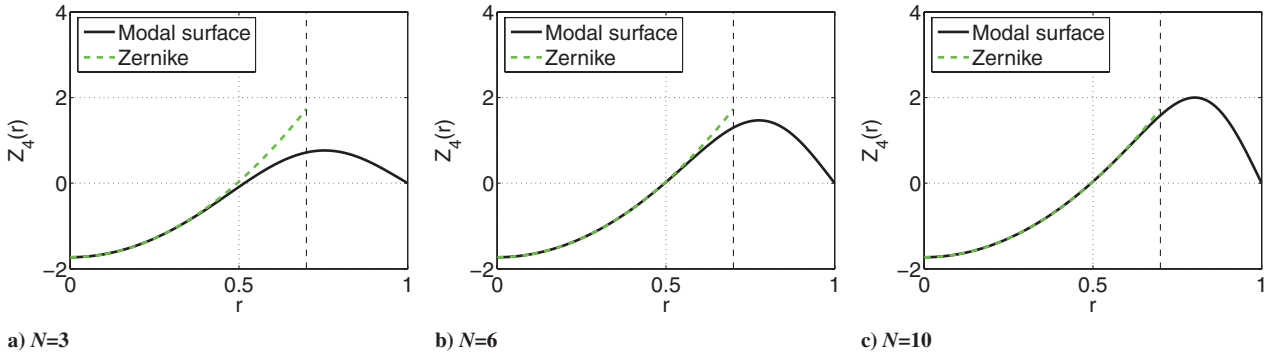


Fig. 6 Impact on the representation of defocus Zernike by varying N .

desired performance. Actuating the number of modes (within the error budget) will be limited by the fineness of the available surface actuators and the computing and energy requirements. With a fixed reflective area predefined, decreasing the clear aperture will effectively increase the radius of the overall structure, with whatever associated weight penalties that entails. However, it is aptly demonstrated that setting a clear-aperture region to an arbitrary value, such as 80%, is neglecting the design optimization that could be performed by the engineer.

VI. Example: Finite Element Model

One of the primary goals of this research was to develop a control methodology for the in-plane-actuated structure. To show the ability of the modal transformation method to perform this function, two case studies in static control are offered.

In the first case study, a 61-actuator finite element model based upon the geometry of a deformable mirror under development at the Air Force Institute of Technology (AFIT) is constructed in MSC.Nastran. Experimental hardware results of 7-actuator versions of the mirror have been previously reported [18–20]. The

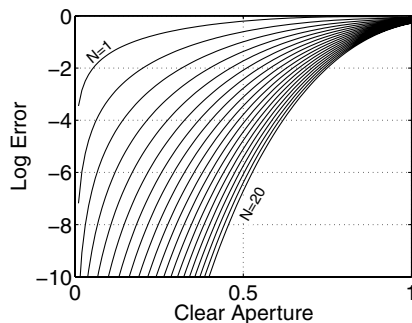


Fig. 7 Surface error of defocus Zernike versus clear aperture with varying N .

developmental-mirror electrode pattern is shown in Fig. 8; however, the hardware example is not as yet fully implemented: thus, the use of finite element models. The modal transformation method is used to form a Zernike-mode surface, and the results are compared with a single iteration of a competing methodology using the projection of the desired surface deflection.

In the second case study, a hypothetical deformable mirror with a finely actuated electrode pattern in which the voltage is variable at every grid point in the finite element model is used to demonstrate the ability of the modal transformation method when used in an iterative scheme to form high-quality low-order axisymmetric and nonsymmetric Zernike modes.

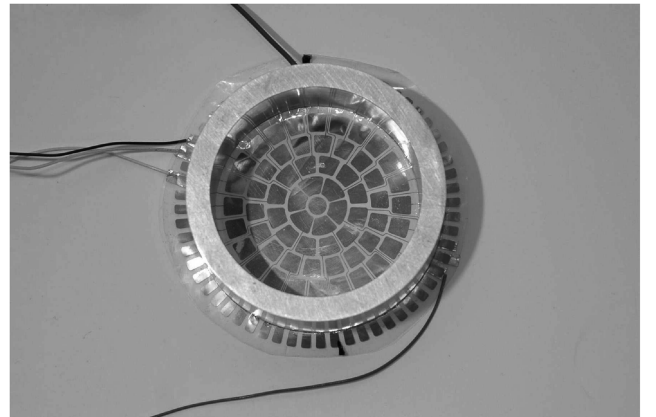


Fig. 8 Example electrode pattern (mirror under development).

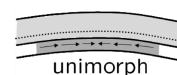


Fig. 9 Piezoelectric in-plane unimorph actuation.

Table 5 Actuator locations for 61-actuator 0.0624-m-radius model

Inner radius, m	Outer radius, m	Azimuthal divisions	Degrees per division
	0.0071	1	360
0.0071	0.0212	6	60
0.0212	0.0353	12	30
0.0353	0.0494	18	20
0.0494	0.0622	24	15

Table 6 Material properties

Parameter	Silicone	PVDF	Units
Young's modulus	1.013	4000	10^6N/m^2
Poisson's ratio	0.497	0.3	—
d_{31}	—	23	$10^{-12}(\text{m/m})/(\text{V/m})$ or $(\text{C/m}^2)/(\text{N/m}^2)$
Thickness	.0015	52.0E – 6	m

The membrane-mirror surface is deflected by the electrode regions by unimorph in-plane actuation. Voltage induces a strain in a piezoelectric-layer offset from the neutral axis, inducing a surface curvature. A visual depiction of the actuating methodology is shown in Fig. 9.

A 61-actuator region is sufficient to show the validity of the control algorithms presented in this paper. In lieu of experimental data, a high-order finite element model of the AFIT deformable mirror was chosen to provide simulated results.

A. Sixty-One-Actuator Finite Element Model

A finite element model of the AFIT deformable mirror testbed was created in MSC.Nastran. The model used the same dimensions as the experimental hardware, except instead of 7 actuating regions as currently configured in the lab, the surface was divided into 61 actuating regions. This increase in actuator density provides greater controllability for this demonstration and is the object of future efforts in experimental designs. The 3601-node model was composed of 3384 CQUAD4 elements and 72 CRIA3 composite-plate elements. The substrate and actuating layers were modeled, and the gold reflective layer and copper–nickel electrode layers were considered to be negligible. Piezoelectric forcing was introduced using the linear piezoelectric-thermal analogy [21] at the locations in Table 5. For the purposes of this example, the directionality of the piezoelectric dielectric constants was removed. Material properties are presented in Table 6.

A uniform edge tension was applied using an enforced-displacement boundary condition in the radial direction. Using a nonlinear static solution, the stiffness of the model was then updated, and an equivalent thermal load was introduced to simulate voltage application at the various actuator locations.

The out-of-plane surface displacements were extracted for analysis. Zernike coefficients were calculated for the area inside of the clear aperture, which could then be used to formulate conclusions about the behavior of various control methodologies.

B. Static Control Methodology for Membrane Mirrors

To provide a competing methodology for computing actuation voltages for static surface control of the Zernike polynomials and to calculate the vibration-mode shapes in this region, the deformable mirror was modeled as a fixed-boundary membrane structure. The forcing functions were modeled to be consistent with existing smart-structure theory, in which the piezoelectric loads are simply line moments acting along the actuator boundary. For a complete derivation of the theory, the reader is referred to Nayfeh and Pai [22]. With plate and nonlinear in-plane tension effects neglected, the governing equation for the deformable mirror with J actuators is

$$T\nabla^2 w(r, \theta) = M\nabla^2 \sum_{i=1}^J F_i(r, \theta) \quad (56)$$

where

$$M = \frac{E}{1-\nu} \frac{d_{31}}{t} \left(-\frac{1}{2} \right) h V_i \quad (57)$$

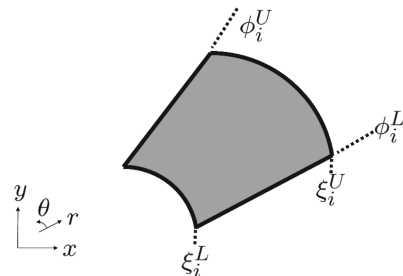
T is membrane tension, E is the substrate modulus, ν is the substrate Poisson constant, d_{31} is the piezoelectric constant, t is the thickness of the piezoelectric layer, h is the distance of the actuator from the composite-structure neutral axis, and V_i is the voltage across the electrodes. Note that we have assumed a negligible structural contribution of the piezoelectric layer to the deformation of the surface.

For our example, F_i is the area of electrode, as shown in Fig. 10. The i th region may be defined through Heaviside functions with radial boundaries ξ_i^U and ξ_i^L and azimuthal boundaries ϕ_i^U and ϕ_i^L :

$$F_i(r, \theta) = \{H(r - \xi_i^L) - H(r - \xi_i^U)\} \cdot \{H(\theta - \phi_i^L) - H(\theta - \phi_i^U)\} \quad (58)$$

Therefore, it is quite obvious that solutions to the partial differential equation are simply a series of scaled-step functions corresponding to the applied voltage on the actuated electrode. We later take advantage of the orthogonal nature of the solution. For a unit voltage, these shapes are defined here as Ψ_i modes. To obtain a desired shape on the membrane surface, it is simply a matter of using the projection theorem to find the individual actuator gains.

For the direct projection method of control, the desired Zernike is constructed directly from the Ψ mode shapes. In the proposed modal transformation method, the Ψ mode shapes are actuated to replicate the membrane vibration-mode shapes, and then the transformation constructs the desired Zernike surface on the clear-aperture region using linear combinations of the approximated vibration-mode shapes. Again, it is emphasized that the modal transformation method always satisfies the fixed-edge boundary conditions, and further limits steep transitions if the Zernike modes are implemented on the interior clear-aperture region.

**Fig. 10** Equation (58) i th actuator boundaries.

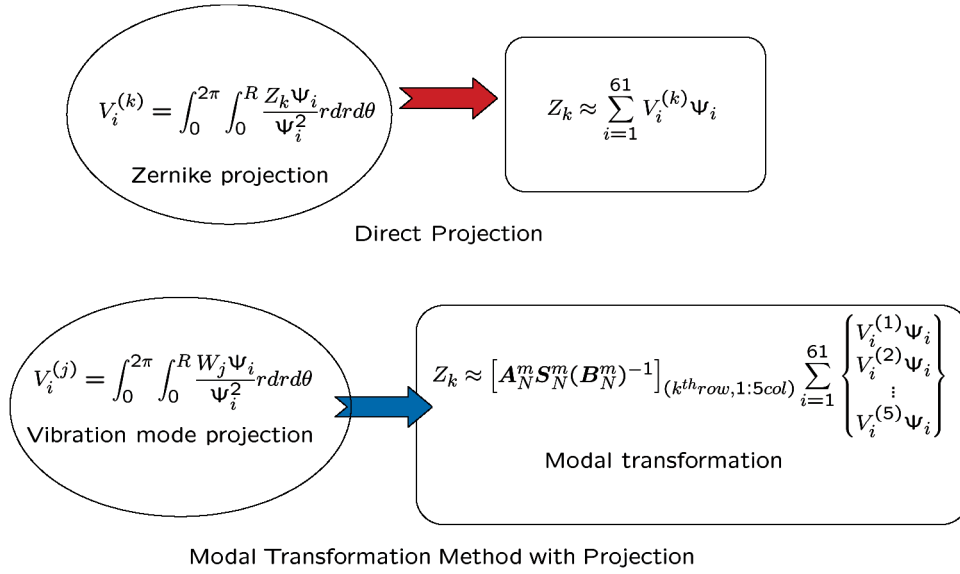


Fig. 11 Pseudocode for computing the voltages in Figs. 12a and 12d.

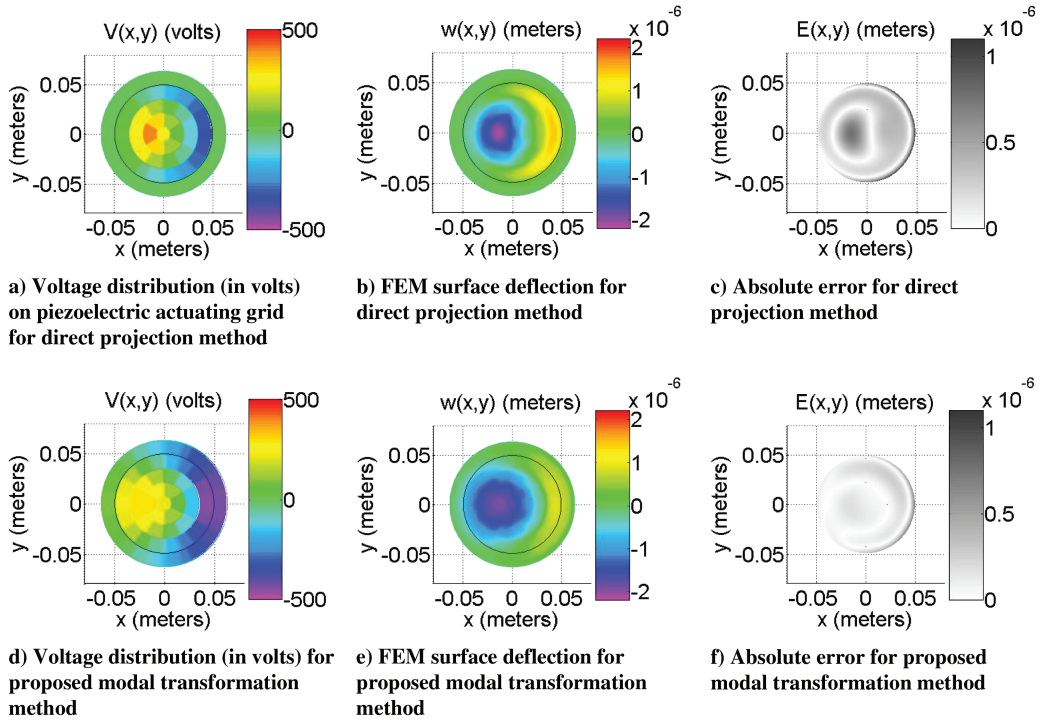


Fig. 12 Direct projection (top) versus modal transformation method (bottom); FEM denotes the finite element model.

C. Static Control Simulation and Results

In the simulation example, voltages were applied to the MSC.Nastran nonlinear finite element model. The desired shape was a simultaneous surface deflection corresponding to the axisymmetric Zernike defocus mode and the nonaxisymmetric tilt mode associated with $\cos(\theta)$. The clear-aperture region was set to 0.78 inside the boundary of the last ring of actuators. A logic flowchart depicts these operations in Fig. 11. In the direct projection method, the Zernike shapes are constructed in the clear aperture from a linear combination of the actuator Ψ modes. In this application of the modal transformation method, the vibration-mode shapes are approximated using the projection theorem to form linear combinations of actuator modes, and then those shapes are used in the modal-transformation-method algorithm using Eqs. (40–42). In the figure, indices i correspond to actuator mode, j correspond to vibration mode, and k

corresponds to the desired Zernike surface. In this modal transformation method, the value of N was set to 20, and the number of actuated vibration modes at a given azimuthal frequency was limited to five. This limit corresponded to the number of actuation rings and thus to the maximum number of zero crossings that was theoretically obtainable. The value of N ensured that the truncation error of Eq. (31) would be negligible.

The voltage inputs $V(x, y)$,** finite-element-model simulation results $w(x, y)$, and absolute-error difference $E(x, y)$ of the desired surface versus the simulated surface are provided for both the direct projection and modal transformation methods for obtaining simultaneous defocus and tilt Zernike-mode shapes across the

**The Cartesian coordinates are used for the plotted surfaces. For translation to cylindrical coordinates (r, θ) , $x = r \cos(\theta)$ and $y = r \sin(\theta)$.

clear-aperture region in Fig. 12. The clear-aperture region is indicated by a black line at 0.78 of the surface radius.

When calculating the voltage inputs for the 61 actuation regions in Figs. 12a and 12d, there was a slight scaling error between the competing methods, and so the voltage was adjusted by a constant to achieve similar deflections. All other responses were linear for the micron-level surface displacements in this simulation, corresponding to input voltages between -500 to 500 V [the practical limit for polyvinylidene difluoride (PVDF) material].

The surface deflection and error plots are compared in the remaining plots of Fig. 12. To calculate surface error, the desired defocus and tilt coefficients were subtracted from the generated surface inside of the clear-aperture region. The piston mode was also neglected: it is of no consequence in optical systems, as it is generally not measurable and does not affect the mirror's optical performance.

Although the absolute-error plots in Fig. 12 give some idea of the performance achievable using the modal transformation method, a breakdown of the surface terms by Zernike coefficients is presented in Figs. 13a and 13b. In both graphs, the desired (and achieved) Zernike coefficient was normalized for approximately 1×10^{-6} to one. The next three Zernike coefficients for the next three higher radial orders at the same azimuthal frequency were then normalized and plotted. The coefficients (and thus contribution to the error) for the sin terms and the higher azimuthal frequency terms (such as $\cos 2\theta$, $\cos 3\theta$, etc.) were not significant and thus are not presented.

When comparing the modal transformation method with the direct projection method in Figs. 13a and 13b, the advantage of the modal transformation method is evident. The error, which shows as nonzero coefficients in the first- and second-higher-order modes of both the symmetric and nonsymmetric modes, is lower for the modal transformation method. Only for the third-highest radial-order mode does the direct projection method show a slight advantage, although the relative error at that high radial frequency in either case is low.

The overall effect is that the modal transformation method may be used to generate Zernike data inside the defined clear-aperture region with less error than when using a competing strategy. The other significant conclusion is that to apply the modal transformation method, actuated regions must occur outside of the clear-aperture region, thus increasing the complexity of the system. In this example, 39% more actuators were required when using the modal transformation method, which would require an attendant amount of power and system integration. However, it is the opinion of the researchers that the performance gain and the resulting decrease in the overall diameter of a mirror structure would far outweigh the increase in complexity. A systems-level trade study is foreseen as a potential future effort.

D. Finely Actuated Finite Element Model

A second finite element model was built to showcase the absolute advantages of the modal transformation method when used in conjunction with a hypothetically achievable in-plane-actuated deformable membrane mirror. For this model, the previous example was modified. The silicone layer was replaced by an inert substrate of thickness and material properties equal to the PVDF layer, resulting in a very thin ($104 \mu\text{m}$ total thickness) mirror. The electrodes were replaced by a voltage distribution field at each finite element grid

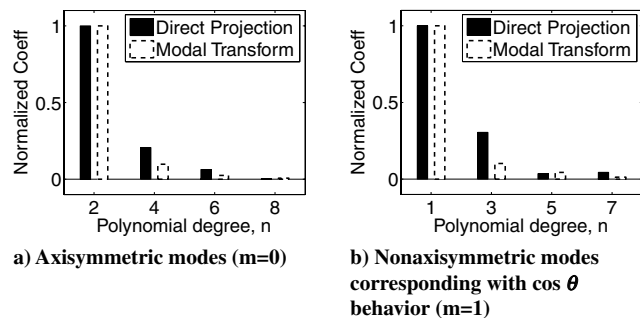


Fig. 13 Comparison of normalized Zernike-mode coefficients.

point, and the number of grid points was increased to 9001. This would be representative of a finely actuated grid such as that conceived to be manufactured with microelectromechanical system techniques or remotely actuated by an electron gun.

A simple iterative technique was used to control the structure, in which the desired Zernike-mode error signal was summed and sent to the modal transformation method to correct voltage fields as the summation of the appropriate Bessel-based mode shapes. Again, the clear aperture was 0.78. The number of actuated modes was $N = 20$.

To obtain a desired bound on the error, it was first necessary to determine the ability of the finite element model to statically replicate the Bessel-based vibration-mode shapes. Voltage patterns $V_n(r, \theta)$ in the form of statically actuated axisymmetric ($m = 0$) Bessel-based vibration-mode shapes were applied: that is,

$$V_n(r, \theta) = 300W_n^0 \quad (59)$$

The surface error of the highest spatial frequency ($N = 20$) was recorded and normalized and then the piston error of 0.42 was removed (note that the error at the fixed boundary was zero before removing this error term). The error is presented in Fig. 14. It was found that the surface error (neglecting piston effects) for the $n = 20$ mode was less than 0.02 times the reference shape inside of a clear aperture of $0.78R$, except in a small region of radius of 0.005 m. In Fig. 7, a similar error of 0.02 for $N = 20$ is also achieved at a clear aperture of 0.78 . Thus, the order of the control system was chosen as $N = 20$, the clear aperture was set to $0.78R$, and the expected performance (assuming that the errors are additive in nature) was to achieve Zernike-mode shapes with error on the order of 0.04 times the commanded shape.

A simple iterative technique was used to control the structure, in which the desired Zernike-mode error signals of the four lowest-order modes were summed and sent to the modal transformation method to correct voltage fields. A schematic of the control diagram is presented in Fig. 15. For the data presented, the iterative loop was allowed to run through four cycles to refine the solutions. Future constructs could be provided to weight the measured Zernike outputs as necessary. This demonstration is intended to show the reduced spillover into other low-order modes, but further proof of convergence or stability is not attempted.

For the simulations, the first four axisymmetric modes ($m = 0$ and $n = \{2, 4, 6, 8\}$) beginning with defocus and the first four nonsymmetric modes [with an azimuthal behavior of $m = 1$, ($\cos \theta$), and $n = \{1, 3, 5, 7\}$] beginning with tilt were commanded. The magnitude of the Zernike polynomials was such that the maximum absolute deflection at the edge of the clear aperture was $1 \mu\text{m}$ (roughly the order of one wavelength of light at 633 nm). The results of this series of simulations are presented in Fig. 16.

From the results presented, it may be seen that the in-plane-actuated mirror can reproduce Zernike surfaces when actuated in

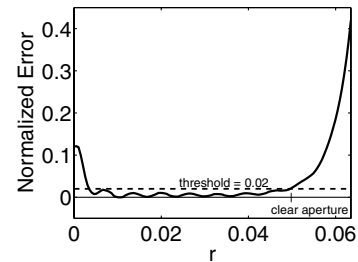


Fig. 14 Twentieth-order Bessel error.

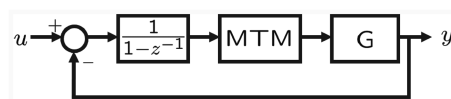


Fig. 15 Feedback algorithm.

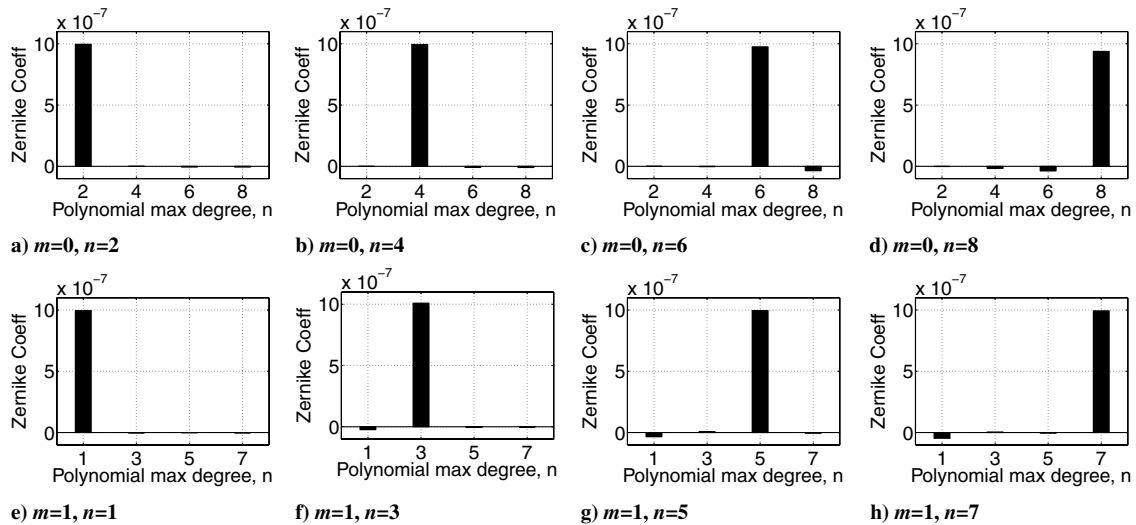


Fig. 16 Closed-loop simulation results.

accordance with the modal transformation method. The greatest absolute error in spillover was found in the Zernike mode corresponding to $m = 1$ and $n = 1$ when the mode $m = 1$ and $n = 7$ was actuated. The value of the absolute error was $0.0475 \mu\text{m}$, very nearly matching the expected absolute error.

VII. Conclusions

The static shape control of a membrane mirror was explored. Development of a methodology that prescribes the desired surface displacement of an interior, clear-aperture region in terms of physically achievable mode shapes was developed. In the development, surface error can be seen to be a function of the clear-aperture radius relative to the mirror radius and as a function of the number and accuracy of achievable mode shapes, themselves functions of the fineness of the actuating grid.

In the example presented, a nonlinear finite-element-model simulation of deformable circular mirror with 61-piezoelectric unimorph actuators showed the advantages of the proposed modal transformation method to determine actuator gains to create a desired surface when compared with a direct projection method based solely on solving the governing membrane equation.

Areas of further research as a direct result of questions posed in this paper include further efforts to accurately (and simply) model the structure to obtain the piezoelectric-actuated vibration-mode shapes essential to the use of this method. Also, the need to invert the modal transformation matrix as presented in Sec. V for higher-order systems may require more advanced techniques.

Despite these areas of further research, the methods presented herein should be suitable for incorporation in the control schemes of larger-scale structures, and although presented for the continuous circular mirror, there is nothing in the method presented that prevents a similar strategy from being developed for annular or parabolic reflectors.

Greater complexity in the system due to the increase in the number of actuators and the subsequent increased power requirement appears to be the main tradeoff for the increased accuracy in quasi-static surface-deflection performance when applying this control methodology.

Acknowledgment

The research presented in this document was conducted with the financial support of the U.S. Air Force Office of Scientific Research under the direction of Sharon Heise.

References

- [1] Agnes, G. S., and Dooley, J., "Precision Deployable Structures Technology for NASA Large Aperture Missions," Space 2004 Conference and Exhibit, AIAA Paper 2004-5889, 2004.
- [2] Acikmese, A., Mettler, E., Breckenridge, W. G., Macenka, S. A., and Tubbs, E. F., "L2 Earth Atmosphere Observatory: Formation Guidance, Metrology, and Control Synthesis," AIAA/AAS Astroautodynamics Specialist Conference and Exhibit, AIAA Paper 2004-5212, 2004.
- [3] Carreras, R. A., "On Near-Net Shape Membrane Optics," AIAA Space Technology Conference and Exposition, AIAA Paper 1999-4642, 1999.
- [4] Ash, J. T., Jenkins, C. H., Marker, D. K., and Wilkes, J. M., "Shape Achievement of Optical Membrane Mirrors Using Coating/Substrate Intrinsic Stresses," *Journal of Spacecraft and Rockets*, Vol. 41, No. 4, 2004, pp. 551–557.
doi:10.2514/1.11936
- [5] Vaughan, H., "Pressurising a Prestretched Membrane to Form a Paraboloid," *International Journal of Engineering Science*, Vol. 18, No. 1, Jan. 1980, pp. 99–107.
doi:10.1016/0020-7225(80)90009-9
- [6] Jenkins, C. H., Wilkes, J. M., and Marker, D. K., "Improved Surface Accuracy of Precision Membrane Reflectors through Adaptive Rim Control," 39th AIAA/ASME/ASCE/AHS/ASC Structures, Structural Dynamics, and Materials Conference, AIAA Paper 1998-1983, 1998.
- [7] Wilkes, J. M., Jenkins, C. H., Marker, D. K., Carreras, R. A., Duneman, D. C., and Rotge, J. R., "Concave Membrane Mirrors from Aspheric to Near-Parabolic," *High-Resolution Wavefront Control: Methods, Devices, and Applications*, edited by J. D. Gonglewski, and M. A. Vorontsov, Vol. 3670, Society of Photo-Optical Instrumentation Engineers, Bellingham, WA, 1999.
- [8] DeSmidt, H. A., Wang, K. W., and Fang, H., "Gore Seam Cable Actuated Shape Control of Integrated Precision Gossamer Reflectors Assessment Study," 47th AIAA/ASME/ASCE/AHS/ASC Structures, Structural Dynamics and Materials Conference, Vol. AIAA Paper 2006-1902, 2006.
- [9] Wang, P. K., and Hadaegh, F. Y., "Modal Noninteracting Controls for Deformable Mirrors," *2nd IEEE Conference on Control Applications*, Vol. 1, Inst. of Electrical and Electronics Engineers, Piscataway, NJ, 1993, pp. 121–128.
- [10] Clafin, E. S., and Bareket, N., "Configuring an Electrostatic Membrane Mirror by Least-Squares Fitting with Analytically Derived Influence Functions," *Journal of the Optical Society of America A (Optics, Image Science and Vision)*, Vol. 3, No. 11, 1986, pp. 1833–1839.
- [11] Tokovinin, A., Thomas, S., and Vdovin, G., "Using 50-mm Electrostatic Membrane Deformable Mirror in Astronomical Adaptive Optics," *Advancements in Adaptive Optics*, edited by D. B. Calia, B. L. Ellerbroek, and R. Ragazzoni, Vol. 5490, Society of Photo-Optical Instrumentation Engineers, Bellingham, WA, 2004, pp. 580–585.
- [12] Flint, E. M., and Denoyer, K. K., "Approach for Efficiently Evaluating Internally Reacted Global Shape Control Actuation Strategies for Apertures," 44th AIAA/ASME/ASCE/AHS/ASC Structures, Structural Dynamics, and Materials Conference, AIAA Paper 2003-1738, 2003.
- [13] Rogers, J. W., and Agnes, G. S., "Modeling Discontinuous Axisymmetric Active Optical Membranes," *Journal of Spacecraft and Rockets*, Vol. 40, No. 4, 2003, pp. 553–564.
doi:10.2514/2.3977

- [14] Pearson, J. E., and Hansen, S., "Experimental Studies of a Deformable Mirror Adaptive Optical System," *Journal of the Optical Society of America*, Vol. 67, No. 3, 1977, pp. 325–333.
- [15] Noll, R. L., "Zernike Polynomials and Atmospheric Turbulence," *Journal of the Optical Society of America*, , Vol. 66, No. 3, 1976, pp. 207–211.
- [16] Meirovitch, L., *Principles and Techniques of Vibrations*, Prentice–Hall, New York, 1997, pp. 439–443.
- [17] Beyer, W. H., editor, *CRC Standard Mathematical Tables*, 28th edition, CRC Press, Boca Raton, FL, 1987, p. 351.
- [18] Wagner, J. W., Agnes, G. S., and Magee, E., "Optical Metrology of Adaptive Membrane Mirrors," *Journal of Intelligent Material Systems and Structures*, Vol. 11, No. 11, 2000, pp. 837–847. doi:10.1106/F47V-LD4V-4YVR-E13G
- [19] Sobers, D. M., Agnes, G. S., and Mollenhauer, D., "Smart Structures for Control of Optical Surfaces," 44th AIAA/ASME/ASCE/AHS/ASC Structures, Structural Dynamics, and Materials Conference, AIAA Paper 2003-1559, 2003.
- [20] Shepherd, M. J., Peterson, G. A., Cobb, R. G., and Palazotto, A. N., "Quasi-Static Optical Control of In-Plane Actuated, Deformable Mirror: Experimental Comparison with Finite Element Analysis," 47th AIAA/ASME/ASCE/AHS/ASC Structures, Structural Dynamics and Materials Conference, AIAA Paper 2006-2231, 2006.
- [21] Cote, F., Masson, P., Mrad, N., and Cotoni, V., "Dynamic and Static Modelling of Piezoelectric Composite Structures Using a Thermal Analogy with MSC/Nastran," *Composite Structures*, Vol. 65, No. 3, 2004, pp. 471–484.
- [22] Nayfeh, A. H., and Pai, P. F., *Linear and Nonlinear Structural Mechanics*, Wiley Series in Nonlinear Science, Wiley-Interscience, New York, 2004, pp. 415–416.